Available online at www.sciencedirect.com
ScienceDirect
Energy Conversion and Management 48 (2007) 2565–2578
ENERGY CONVERSION & MANAGEMENT
www.elsevier.com/locate/enconman

Control oriented 1D electrochemical model of lithium ion battery

Kandler A. Smith [a], Christopher D. Rahn [b,*], Chao-Yang Wang [b]

[a] Center for Transportation Technologies and Systems, National Renewable Energy Laboratory, Golden, CO 80401, USA
[b] Department of Mechanical and Nuclear Engineering, The Pennsylvania State University, University Park, PA 16802, USA

Received 1 August 2006; accepted 29 March 2007
Available online 28 June 2007

Abstract

Lithium ion (Li-ion) batteries provide high energy and power density energy storage for diverse applications ranging from cell phones to hybrid electric vehicles (HEVs). For efficient and reliable systems integration, low order dynamic battery models are needed. This paper introduces a general method to generate numerically a fully observable/controllable state variable model from electrochemical kinetic, species and charge partial differential equations that govern the discharge/charge behavior of a Li-ion battery. Validated against a 313th order nonlinear CFD model of a 6 Ah HEV cell, a 12th order state variable model predicts terminal voltage to within 1% for pulse and constant current profiles at rates up to 50 C. The state equation is constructed in modal form with constant negative real eigenvalues distributed in frequency space from 0 to 10 Hz. Open circuit potential, electrode surface concentration/reaction distribution coupling and electrolyte concentration/ionic conductivity nonlinearities are explicitly approximated in the model output equation on a local, electrode-averaged and distributed basis, respectively. The balanced realization controllability/observability gramian indicates that the fast electrode surface concentration dynamics are more observable/controllable than the electrode bulk concentration dynamics (i.e. state of charge).

Keywords: Lithium ion battery; Electrochemical model; State of charge estimation; Hybrid electric vehicle; Distributed parameter model order reduction

1. Introduction

Batteries directly contribute to the advancement of technologies ranging from portable electronics to fuel efficient vehicles. Model based battery monitoring algorithms, of particular importance in high power applications, use current and voltage measurements to estimate state of charge (SOC), available power and state of health (SOH) with interacting systems basing control action upon these estimates [1,2]. Despite increased cost, hybrid power system designs must often employ conservative, oversized batteries due to imprecise estimations. Development of an accurate online dynamic battery model is difficult given the nonlinear, infinite dimensional, distributed mass transport processes governing electrochemical system dynamics [3,4]. Empirical battery models are often favored for their low order (2–5 states) and relative ease of identification [1,5,6]. Fundamental models, presumably offering better accuracy, are rarely employed in real time due to their high order (30–100 states) [7,8]. The objective of the present work is to develop a fundamental lithium-ion (Li-ion) battery model in a low order state variable form that is practical for real time application.

Diffusive mass transport processes, with an infinite number of negative real eigenvalues [9], cause batteries to respond across a range of time scales. Karden et al. report battery dynamics as slow as 35 μHz [10], while at very high rates, Smith and Wang show that a hybrid electric vehicle (HEV) cell may become solid state diffusion limited in seconds [11]. Equivalent circuit models with just 2–3 states cannot be expected to predict accurately the current/voltage behavior across such disparate time scales. By neglecting fast dynamics however, these empirical models may accurately predict low rate discharge behavior [12], or, by neglecting slow dynamics, high rate perturbations within

* Corresponding author. Tel.: +1 814 865 6237; fax: +1 814 863 7222.
E-mail address: cdrahn@psu.edu (C.D. Rahn).

0196-8904/$ - see front matter © 2007 Elsevier Ltd. All rights reserved.
doi:10.1016/j.enconman.2007.03.015

a small SOC range [13]. In the literature, empirical model parameters are commonly fitted to a representative data set with little discussion of model bandwidth and region of validity (SOC range, admissible current inputs etc.). In addition, these models can only be used after a battery has been built and tested and are unavailable during the design process.

Fundamental battery models, derived for the Li-ion chemistry from porous electrode and concentrated solution theories [14,15], mathematically describe charge and species transport in the solid (electrode active material) and electrolyte phases across a simplified 1D cell structure. Solved numerically in a computational fluid dynamics (CFD) framework, the coupled partial differential equations (PDEs) are spatially discretized (via finite difference, Galerkin or similar method) and the resulting set of ordinary differential equations (ODEs) is solved iteratively. For real time applications, slow and possibly non-convergent execution is unacceptable, and a fast and reliable approximate model is sought. Tenno et al. [7] sequentially solve diagonal ODE systems representing lead acid battery distributed concentrations/potentials and use a PID (proportional-integral-derivative) controller to tune model states to match current/voltage measurements during slow discharge. For nickel metal-hydride battery SOC estimation, Barbarisi et al. [8] neglect the electrolyte phase and negative electrode solid state transport, assume uniform reaction current and discretize the positive electrode solid state diffusion PDE to a 32nd order system of ODEs. Model order reduction techniques, performed in the time [16,17] or frequency [9] domain, offer potential to reduce further the model order and avoid restrictive assumptions.

In this paper, Section 2 summarizes the 1D electrochemical model equations and derives an impedance (frequency domain) model under the assumptions of quasi-linear behavior and local reaction current decoupled from electrolyte concentration. Section 3 reduces the impedance model transfer functions/matrices to low order SIMO (single input multiple output) state variable models (SVMs) [9]. Section 4 presents SVM simulation results for a 6 Ah Li-ion HEV cell, comparing internal reaction and concentration distributions and external current/voltage behavior to a high order nonlinear CFD model [11].

2. Model

Fig. 1 shows a schematic of the Li-ion cell consisting of three domains: the negative composite electrode, separator and positive composite electrode. During discharge, Li ions diffuse to the surface of Li_xC_6 active material particles

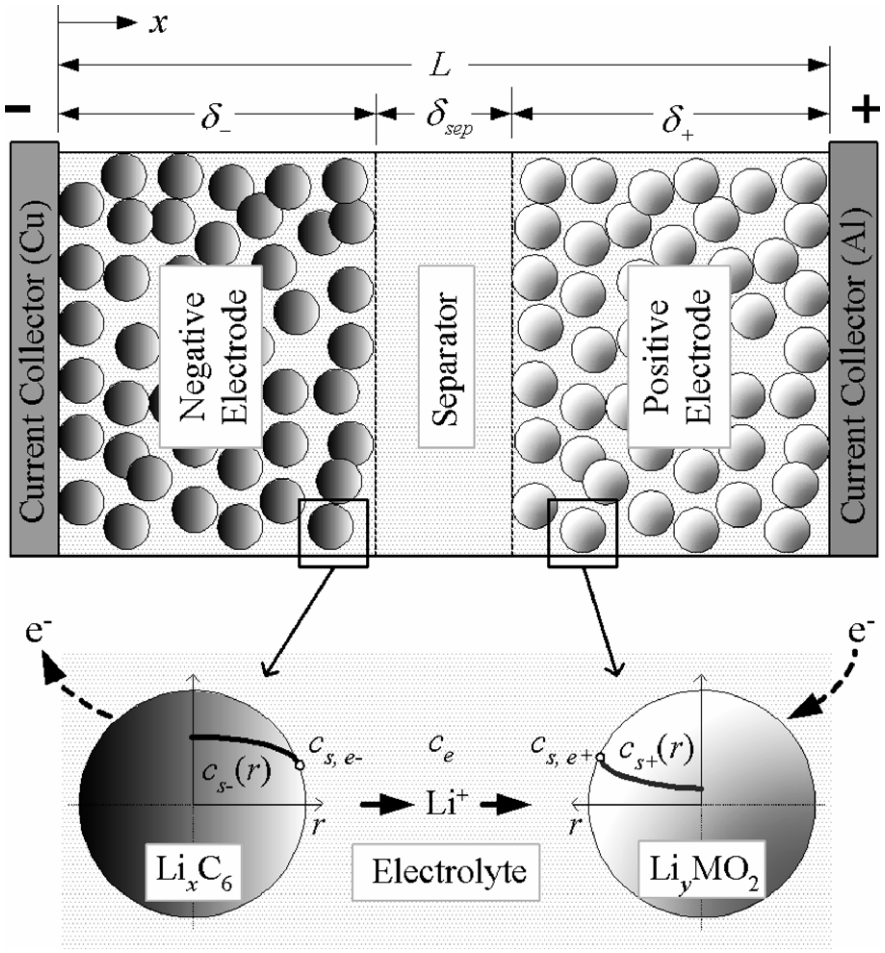

Fig. 1. Schematic of a Li-ion cell.

(solid phase) in the negative electrode where they undergo electrochemical reaction and transfer into a liquid or gelled electrolyte solution (electrolyte phase). The positively charged ions travel through the electrolyte solution via diffusion and ionic conduction to the positive electrode where they react and diffuse towards the inner regions of metal oxide active material particles (solid phase). The porous separator serves as an electronic insulator, forcing electrons to follow an opposite path through an external circuit or load. Both composite electrodes contain binder and filler (not shown in Fig. 1) to enhance electron transport across the solid matrix. End of discharge/charge, accompanied by sudden voltage decay/rise, occurs when the solid phase Li concentrations at either electrode surface become saturated or depleted, or electrolyte phase Li concentration becomes depleted in either electrode.

2.1. Governing equations

We provide a brief summary of the model governing equations derived in Refs. [14,15] and applied in Ref. [11]. Composite electrodes are modeled using porous electrode theory, meaning that the solid and electrolyte phases are treated as superimposed continua without regard to microstructure. Conservation of Li in a single spherical active material particle is described by Ficks law of diffusion,

$$\frac{\partial c_s}{\partial t} = \frac{D_s}{r^2}\frac{\partial}{\partial r}\left(r^2\frac{\partial c_s}{\partial r}\right), \tag{1}$$

with boundary conditions

$$\left.\frac{\partial c_s}{\partial r}\right|_{r=0} = 0 \tag{2}$$

$$\left.D_s\frac{\partial c_s}{\partial r}\right|_{r=R_s} = \frac{-j^{Li}}{a_s F}. \tag{3}$$

In Eqs. (1)–(3), c represents Li concentration, and the subscript s denotes the solid phase. D_s is the solid phase diffusion coefficient, j^{Li} the volumetric rate of electrochemical reaction at the particle surface (with $j^{Li} > 0$ indicating ion discharge), a_s the specific interfacial surface area and F is Faraday's constant (96,487 C/mol). For spherical active material particles of radius R_s occupying electrode volume fraction ε_s, the interfacial surface area is $a_s = 3\varepsilon_s/R_s$. Eqs. (1)–(3) are applied on a continuum basis across each electrode, giving the solid phase concentration a 2D spatial dependency, i.e. $c_s(x, r, t)$ where x is the particle position, r is the radial position within a particle and t is time. The electrochemical model depends only upon concentration at the particle surface, $c_{s,e}(x, t) = c_s(x, R_s, t)$, where the subscript s, e denotes the solid/electrolyte interface.

Conservation of Li in the electrolyte phase yields

$$\frac{\partial(\varepsilon_e c_e)}{\partial t} = \frac{\partial}{\partial x}\left(D_e^{eff}\frac{\partial}{\partial x}c_e\right) + \frac{1-t_+^0}{F}j^{Li} \tag{4}$$

with zero flux boundary conditions at the current collectors,

$$\left.\frac{\partial c_e}{\partial x}\right|_{x=0} = \left.\frac{\partial c_e}{\partial x}\right|_{x=L} = 0 \tag{5}$$

where $c_e(x, t)$ is electrolyte phase Li concentration, ε_e is electrolyte phase volume fraction and t_+^0 is the transference number of Li^+ with respect to the velocity of solvent. The effective diffusion coefficient is calculated from a reference coefficient using the Bruggeman relation $D_e^{eff} = D_e\varepsilon_e^p$ that accounts for the tortuous path that Li^+ ions follow through the porous media. Eq. (4) assumes constant t_+^0.

Charge conservation in the solid phase of each electrode is described by Ohm's law

$$\frac{\partial}{\partial x}\left(\sigma^{eff}\frac{\partial}{\partial x}\phi_s\right) - j^{Li} = 0 \tag{6}$$

with boundary conditions at the current collectors proportional to applied current,

$$-\sigma_-^{eff}\left.\frac{\partial\phi_s}{\partial x}\right|_{x=0} = \sigma_+^{eff}\left.\frac{\partial\phi_s}{\partial x}\right|_{x=L} = \frac{I}{A}, \tag{7}$$

and zero electronic current at the separator,

$$\left.\frac{\partial\phi_s}{\partial x}\right|_{x=\delta_-} = \left.\frac{\partial\phi_s}{\partial x}\right|_{x=\delta_-+\delta_{sep}} = 0. \tag{8}$$

In Eqs. (6)–(8), $\phi_s(x, t)$ and σ^{eff} are the potential and effective conductivity of the solid matrix, respectively, with σ^{eff} evaluated from the active material reference conductivity σ as $\sigma^{eff} = \sigma\varepsilon_s$. A is electrode plate area, and $I(t)$ is the applied current following the sign convention that a positive current discharges the battery.

Electrolyte phase charge conservation yields

$$\frac{\partial}{\partial x}\left(\kappa^{eff}\frac{\partial}{\partial x}\phi_e\right) + \frac{\partial}{\partial x}\left(\kappa_D^{eff}\frac{\partial}{\partial x}\ln c_e\right) + j^{Li} = 0 \tag{9}$$

with boundary conditions

$$\left.\frac{\partial\phi_e}{\partial x}\right|_{x=0} = \left.\frac{\partial\phi_e}{\partial x}\right|_{x=L} = 0. \tag{10}$$

In Eqs. (9), (10), $\phi_e(x, t)$ is the electrolyte phase potential and κ^{eff} the effective ionic conductivity, calculated from the Bruggeman relation $\kappa^{eff} = \kappa\varepsilon_e^p$. Derived from concentrated solution theory, the effective diffusional conductivity is

$$\kappa_D^{eff} = \frac{2RT\kappa^{eff}}{F}(t_+^0 - 1)\left(1 + \frac{d\ln f_\pm}{d\ln c_e}\right) \tag{11}$$

where R is the universal gas constant (8.3143 J/mol K), T is temperature and $f_\pm$ is the activity coefficient, assumed in the present work to be constant.

The four governing PDEs (1), (4), (6) and (9) describing field variables, $c_{s,e}$, c_e, ϕ_s and ϕ_e, are coupled by the Butler–Volmer electrochemical kinetic expression

$$j^{Li} = a_s i_0\left\{\exp\left[\frac{\alpha_a F}{RT}\eta\right] - \exp\left[-\frac{\alpha_c F}{RT}\eta\right]\right\}. \tag{12}$$

In Eq. (12), j^{Li} is driven by overpotential, η, defined as the difference between solid and electrolyte phase potentials minus the thermodynamic equilibrium potential, U, of the solid phase

$$\eta = \phi_s - \phi_e - U. \tag{13}$$

Equilibrium potential, $U(c_{s,e})$, is evaluated as a function of the solid phase concentration at the particle surface. In Eq. (12), exchange current density, i_0, is related to both solid surface and electrolyte concentrations according to

$$i_0 = k(c_e)^{\alpha_a}(c_{s,\max} - c_{s,e})^{\alpha_a}(c_{s,e})^{\alpha_c} \tag{14}$$

where k is a kinetic rate constant, and α_a and α_c are the anodic and cathodic transfer coefficients, respectively.

With boundary conditions applied galvanostatically, Eq. (7), the cell current, $I(t)$, is the model input. Voltage across the cell terminals is calculated as

$$V(t) = \phi_s(L,t) - \phi_s(0,t) - \frac{R_f}{A}I(t) \tag{15}$$

where R_f is an empirical contact resistance. The nonlinear governing PDEs and constitutive relationships are numerically solved within a computational fluid dynamics (CFD) framework as described in Ref. [11]. In Section 4, this "CFD model" is used to assess the accuracy of low order SVMs.

2.2. Impedance model formulation

We manipulate the governing equations to derive analytical transfer functions in Section 2.2.1 and numerical transfer matrices in Section 2.2.2 describing the output response of the impedance model field variables $\bar{c}_{s,e}(x,s)$, $\bar{c}_e(x,s)$, $\bar{\phi}_s(x,s)$ and $\bar{\phi}_e(x,s)$ to an input current, $\bar{I}(s)$. Individual submodel responses are combined to form the voltage response, $\overline{V}(s)$, in Section 2.2.3. In preparation for the model order reduction procedure (introduced in Section 3), we modify the transfer functions/matrices as necessary to give them finite steady state solutions. The impedance model assumptions are:

(i) Linear behavior (i.e. constant properties), and
(ii) Reaction current, $\bar{j}^{Li}(x,s)$, decoupled from electrolyte concentration, $\bar{c}_e(x,s)$.

For other fundamental impedance models, see Refs. [18–20] and the references therein.

2.2.1. Electrode submodel

Taking the Laplace transform of Eq. (1) and solving it with respect to boundary conditions equations (2) and (3), Jacobsen and West [19] give the solid state diffusion impedance of a spherical active material particle

$$\frac{\bar{c}_{s,e}(s)}{\bar{j}^{Li}(s)} = \frac{1}{a_s F}\left(\frac{R_s}{D_s}\right)\left[\frac{\tanh(\beta)}{\tanh(\beta)-\beta}\right], \tag{16}$$

where $\beta = R_s\sqrt{s/D_s}$. Linearization of the Butler–Volmer kinetic relationship equation (12) yields

$$\bar{\eta} = \frac{R_{ct}}{a_s}\bar{j}^{Li} \tag{17}$$

with charge transfer resistance, $R_{ct} = RT/[i_0F(\alpha_a + \alpha_c)]$.

Define the dimensionless spatial variable $z = x/\delta$, where δ is the electrode thickness, $z = 0$ represents the current collector interface and $z = 1$ represents the separator interface. The solid phase charge conservation equation (6) linearized and expressed as a function of z, is

$$\frac{\sigma^{eff}}{\delta^2}\frac{\partial^2\bar{\phi}_s}{\partial z^2} - \bar{j}^{Li} = 0 \tag{18}$$

with boundary conditions

$$-\frac{\sigma^{eff}}{\delta}\frac{\partial\bar{\phi}_s}{\partial z}\bigg|_{z=0} = \frac{\bar{I}}{A} \tag{19}$$

$$\frac{\partial\bar{\phi}_s}{\partial z}\bigg|_{z=1} = 0 \tag{20}$$

Consistent with assumption (ii), we neglect the 2nd term on the left hand side of electrolyte charge conservation equation (9) and assume constant κ^{eff}, yielding

$$\frac{\kappa^{eff}}{\delta^2}\frac{\partial^2\bar{\phi}_e}{\partial z^2} + \bar{j}^{Li} = 0 \tag{21}$$

with boundary conditions

$$\frac{\partial\bar{\phi}_e}{\partial z}\bigg|_{z=0} = 0, \tag{22}$$

$$\frac{\kappa^{eff}}{\delta}\frac{\partial\bar{\phi}_e}{\partial z}\bigg|_{z=1} = \frac{\bar{I}}{A}. \tag{23}$$

We subtract Eqs. (21)–(23) from Eqs. (18)–(20) to arrive at a single static ODE for phase potential difference, $\phi_{s-e} = \phi_s - \phi_e$,

$$\frac{\partial^2\bar{\phi}_{s-e}}{\partial z^2} = \delta^2\left(\frac{1}{\kappa^{eff}} + \frac{1}{\sigma^{eff}}\right)\bar{j}^{Li} \tag{24}$$

with boundary conditions

$$-\frac{\sigma^{eff}}{\delta}\frac{\partial\bar{\phi}_{s-e}}{\partial z}\bigg|_{z=0} = \frac{\kappa^{eff}}{\delta}\frac{\partial\bar{\phi}_{s-e}}{\partial z}\bigg|_{z=1} = \frac{\bar{I}}{A}. \tag{25}$$

Phase potential difference may be expressed as a function of overpotential, and thus reaction rate, as

$$\bar{\phi}_{s-e} = \bar{\eta} - \overline{U} = \frac{R_{ct}}{a_s}\bar{j}^{Li} - \overline{U} \tag{26}$$

Express the equilibrium potential impedance using the diffusional impedance transfer function equation (16) to yield

$$\bar{\phi}_{s-e}(s) = \left[\frac{R_{ct}}{a_s} + \frac{\partial U}{\partial c_s}\left(\frac{\bar{c}_{s,e}(s)}{\bar{j}^{Li}(s)}\right)\right]\bar{j}^{Li}(s), \tag{27}$$

valid for small perturbations in $c_{s,e}$ where $\partial U/\partial c_s$ is approximately constant. Combining Eq. (27) with Eq. (24), we eliminate $\bar{j}^{Li}$ to obtain an ODE in $\bar{\phi}_{s-e}$

$$\frac{\partial^2\bar{\phi}_{s-e}(z,s)}{\partial z^2} = \delta^2\left(\frac{1}{\kappa^{eff}} + \frac{1}{\sigma^{eff}}\right)\left[\frac{R_{ct}}{a_s} + \frac{\partial U}{\partial c_s}\left(\frac{\bar{c}_{s,e}(s)}{\bar{j}^{Li}(s)}\right)\right]^{-1}\bar{\phi}_{s-e}(z,s) \tag{28}$$

with boundary conditions

$$-\frac{\sigma^{\text{eff}}}{\delta}\left.\frac{\partial\bar{\phi}_{\text{s-e}}(z,s)}{\partial z}\right|_{z=0}=\frac{\kappa^{\text{eff}}}{\delta}\left.\frac{\partial\bar{\phi}_{\text{s-e}}(z,s)}{\partial z}\right|_{z=1}=\frac{\bar{I}(s)}{A}. \tag{29}$$

Eqs. (28) and (29) may now be solved analytically to provide distributed transfer functions for physiochemical variables. Define dimensionless variable v as

$$v(s)=\delta\left(\frac{1}{\kappa}+\frac{1}{\sigma}\right)^{\frac{1}{2}}\left(\frac{R_{\text{ct}}}{a_{\text{s}}}+\frac{\partial U}{\partial c_{\text{s}}}\left(\frac{\bar{c}_{\text{s,e}}(s)}{\bar{j}^{\text{Li}}(s)}\right)\right)^{-\frac{1}{2}} \tag{30}$$

and we have transcendental transfer functions

$$\begin{aligned}\frac{\bar{\phi}_{\text{s-e}}(z,s)}{\bar{I}(s)}&=\frac{1}{A}\frac{\delta}{v(s)\sinh v(s)}\\&\quad\times\left\{\frac{1}{\sigma^{\text{eff}}}\cosh\left[v(s)(z-1)\right]\right.\\&\quad\left.+\frac{1}{\kappa^{\text{eff}}}\cosh[v(s)(z)]\right\}\end{aligned} \tag{31}$$

$$\begin{aligned}\frac{\bar{j}^{\text{Li}}(z,s)}{\bar{I}(s)}&=\frac{\bar{j}^{\text{Li}}(s)}{\bar{\phi}_{\text{s-e}}(s)}\frac{\bar{\phi}_{\text{s-e}}(z,s)}{\bar{I}(s)}\\&=\frac{1}{\delta A}\frac{1}{\kappa^{\text{eff}}+\sigma^{\text{eff}}}\frac{v(s)}{\sinh v(s)}\{\kappa^{\text{eff}}\cosh[v(s)(z-1)]\\&\quad+\sigma^{\text{eff}}\cosh[v(s)(z)]\}\end{aligned} \tag{32}$$

$$\frac{\bar{\eta}(z,s)}{\bar{I}(s)}=\frac{R_{\text{ct}}}{a_{\text{s}}}\frac{\bar{j}^{\text{Li}}(z,s)}{\bar{I}(s)} \tag{33}$$

$$\frac{\Delta\bar{c}_{\text{s,e}}(z,s)}{\bar{I}(s)}=\frac{\bar{c}_{\text{s,e}}(s)}{\bar{j}^{\text{Li}}(s)}\frac{\bar{j}^{\text{Li}}(z,s)}{\bar{I}(s)}-\frac{\bar{c}_{\text{s,avg}}(s)}{\bar{I}(s)} \tag{34}$$

where, in Eq. (34), the bulk electrode solid phase concentration response is

$$\frac{\bar{c}_{\text{s,avg}}(s)}{\bar{I}(s)}=-\frac{1}{\delta A\varepsilon_{\text{s}}F}\frac{1}{s}. \tag{35}$$

Eqs. (31)–(34) have finite steady state and negative real eigenvalues. By defining solid surface concentrations as the difference $\Delta c_{\text{s,e}}(z,t)=c_{\text{s,e}}(z,t)-c_{\text{s,avg}}(t)$, we have removed an eigenvalue at the origin from $\bar{c}_{\text{s,e}}(z,s)/\bar{I}(s)$. Eqs. (31)–(35) are written for the negative electrode. To obtain transfer functions for the positive electrode, multiply by -1. Ong and Newmann [20] present a similar solution to Eq. (31) including high frequency double layer capacitance dynamics but neglecting low frequency diffusional impedance. The double layer capacitive effect, relevant on the millisecond time scale, may be included in Eqs. (31)–(34) with minor modification of Eq. (30), necessary only if the desired battery model bandwidth is greater than ~100 Hz.

2.2.2. Electrolyte submodel

The previous section derived analytical transfer functions in a single electrode region. In electrolyte phase conservation equations (4) and (9), parameters ε_{e}, κ^{eff} and $D_{\text{e}}^{\text{eff}}$ take on different values in the negative electrode, separator and positive electrode regions, making analytical treatment cumbersome. We use the finite element method to obtain spatially discretized transfer matrices with solutions at node points x_i across the 1D domain.

The source term $j^{\text{Li}}(x,t)$ in Eqs. (4) and (9) is approximated as the $n_{cell}\times 1$ vector $\mathbf{j}^{\text{Li}}(t)$. The Laplace transform of $\mathbf{j}^{\text{Li}}(t)$ is constructed by applying Eq. (32) at discrete locations in the negative and positive (with proper sign) electrodes and setting separator node points to zero

$$\begin{aligned}\bar{\mathbf{j}}^{\text{Li}}(s)=[&\bar{j}_{-}^{\text{Li}}(x_1,s),\ldots,\bar{j}_{-}^{\text{Li}}(x_{n_-},s),0,\ldots,0,\bar{j}_{+}^{\text{Li}}(x_{n_{\text{cell}}-n_++1},s),\\&\ldots,\bar{j}_{+}^{\text{Li}}(x_{n_{\text{cell}}},s)]^{\text{T}}.\end{aligned} \tag{36}$$

Finite element discretization of the electrolyte phase diffusion equation (4) yields

$$\mathbf{M}_{c_{\text{e}}}\dot{\mathbf{c}}_{\text{e}}(t)=-\mathbf{K}_{c_{\text{e}}}\mathbf{c}_{\text{e}}(t)+\mathbf{F}_{c_{\text{e}}}\mathbf{j}^{\text{Li}}(t) \tag{37}$$

where $\mathbf{M}_{c_{\text{e}}}$, $\mathbf{K}_{c_{\text{e}}}$ and $\mathbf{F}_{c_{\text{e}}}$ are the mass, stiffness and forcing matrices, respectively [21]. Laplace transform of Eq. (37) yields the transfer matrix

$$\frac{\bar{\mathbf{c}}_{\text{e}}(s)}{\bar{I}(s)}=(\mathbf{K}_{c_{\text{e}}}+s\mathbf{M}_{c_{\text{e}}})^{-1}\mathbf{F}_{c_{\text{e}}}\frac{\bar{\mathbf{j}}^{\text{Li}}(s)}{\bar{I}(s)}. \tag{38}$$

Eq. (38) contains an eigenvalue/zero cancellation at the origin, which we eliminate by defining $\Delta c_{\text{e}}(x,t)=c_{\text{e}}(x,t)-c_{\text{e}}(0,t)$. The transfer matrix

$$\frac{\Delta\bar{\mathbf{c}}_{\text{e}}(s)}{\bar{I}(s)}=\frac{\bar{\mathbf{c}}_{\text{e}}(s)}{\bar{I}(s)}-\frac{\bar{c}_{\text{e}}(0,s)}{\bar{I}(s)} \tag{39}$$

contains no eigenvalue/zero at the origin. Following reduction, $c_{\text{e}}(x,t)$ is recovered by enforcing charge conservation across the cell to find $c_{\text{e}}(0,t)$,

$$c_{\text{e}}(0,t)=c_{e,0}-\frac{1}{L}\int_0^L\Delta c_{\text{e}}(x,t)\,\text{d}x. \tag{40}$$

The electrolyte phase charge conservation equation (9) is linearized to

$$\kappa^{\text{eff}}\frac{\partial^2\phi_{\text{e}}}{\partial x^2}+\frac{\kappa_D^{\text{eff}}}{c_{e,0}}\frac{\partial^2 c_{\text{e}}}{\partial x^2}+j^{\text{Li}}=0 \tag{41}$$

and spatially discretized to

$$-\mathbf{K}_{\phi_{\text{e}}^I}\boldsymbol{\varphi}_{\text{e}}(t)-\mathbf{K}_{\phi_{\text{e}}^{II}}\mathbf{c}_{\text{e}}(t)+\mathbf{F}_{\phi_{\text{e}}}\mathbf{j}^{\text{Li}}(t)=0. \tag{42}$$

The electrolyte phase potential, having no absolute reference, is given one by defining $\Delta\phi_{\text{e}}(x,t)=\phi_{\text{e}}(x,t)-\phi_{\text{e}}(0,t)$, thus fixing $\Delta\phi_{\text{e}}(0,t)=0$. We subtract the (1, 1) element of $\mathbf{K}_{\phi_{\text{e}}^I}$ in Eq. (42) from the first column of all rows of $\mathbf{K}_{\phi_{\text{e}}^I}$,

$$\mathbf{K}_{\Delta\phi_{\text{e}}^I}=\mathbf{K}_{\phi_{\text{e}}^I}-(\mathbf{K}_{\phi_{\text{e}}^I})_{1,1}\begin{bmatrix}1&0&\cdots&0\\1&0&&\\\vdots&&\ddots&\\1&0&\cdots&0\end{bmatrix}, \tag{43}$$

to produce a transfer matrix approximating $\Delta\bar{\phi}_{\text{e}}(x,s)$ at discrete node points x_i,

$$\frac{\Delta\bar{\boldsymbol{\varphi}}_{\text{e}}(s)}{\bar{I}(s)}=(\mathbf{K}_{\Delta\phi_{\text{e}}^I})^{-1}\left(-\mathbf{K}_{\phi_{\text{e}}^{II}}\frac{\Delta\bar{\mathbf{c}}_{\text{e}}(s)}{\bar{I}(s)}+\mathbf{F}_{\phi_{\text{e}}}\frac{\bar{\mathbf{j}}^{\text{Li}}(s)}{\bar{I}(s)}\right). \tag{44}$$

2.2.3. Current/voltage model

Substituting Eq. (13) into Eq. (15), the voltage equation is expanded as

$$V(t) = \phi_e(L,t) - \phi_e(0,t) + \eta(L,t) - \eta(0,t) + U_+(c_{s,e}(L,t)) - U_-(c_{s,e}(0,t)) - \frac{R_f}{A} I(t). \quad (45)$$

After Laplace transform, the voltage response of the linear impedance model is

$$\frac{\overline{V}(s)}{\overline{I}(s)} = \frac{\overline{V}_{OC}(s)}{\overline{I}(s)} + \frac{\overline{V}_-(s)}{\overline{I}(s)} + \frac{\overline{V}_+(s)}{\overline{I}(s)} + \frac{\overline{V}_e(s)}{\overline{I}(s)} - \frac{R_f}{A} \quad (46)$$

with individual terms arising due to bulk concentration, or open circuit voltage dynamics,

$$\frac{\overline{V}_{OC}(s)}{\overline{I}(s)} = \frac{\partial U_+}{\partial c_{s+}} \frac{\bar{c}_{s,avg+}(s)}{\overline{I}(s)} - \frac{\partial U_-}{\partial c_{s-}} \frac{\bar{c}_{s,avg-}(s)}{\overline{I}(s)} = \frac{1}{AF}\left[\frac{\partial U_+}{\partial c_{s+}} \frac{1}{\delta_+ \varepsilon_{s+}} - \frac{\partial U_-}{\partial c_{s-}} \frac{1}{\delta_- \varepsilon_{s-}}\right] \frac{1}{s}, \quad (47)$$

negative electrode solid state diffusion dynamics,

$$\frac{\overline{V}_-(s)}{\overline{I}(s)} = -\frac{\partial U_-}{\partial c_{s-}} \frac{\Delta \bar{c}_{s,e-}(0,s)}{\overline{I}(s)} - \frac{\bar{\eta}_-(0,s)}{\overline{I}(s)} + \frac{\Delta \bar{\phi}_e^{j_-^{Li}}(L,s)}{\overline{I}(s)}, \quad (48)$$

positive electrode solid state diffusion dynamics,

$$\frac{\overline{V}_+(s)}{\overline{I}(s)} = +\frac{\partial U_+}{\partial c_{s+}} \frac{\Delta \bar{c}_{s,e+}(0,s)}{\overline{I}(s)} + \frac{\bar{\eta}_+(0,s)}{\overline{I}(s)} + \frac{\Delta \bar{\phi}_e^{j_+^{Li}}(L,s)}{\overline{I}(s)}, \quad (49)$$

and electrolyte phase diffusion dynamics,

$$\frac{\overline{V}_e(s)}{\overline{I}(s)} = \frac{\Delta \bar{\phi}_e^{\Delta c_e}(L,s)}{\overline{I}(s)}. \quad (50)$$

In defining Eqs. (48)–(50), we have used superposition to break up Eq. (44) into individual components $\Delta\bar{\phi}_e^{j_-^{Li}}$, $\Delta\bar{\phi}_e^{j_+^{Li}}$ and $\Delta\bar{\phi}_e^{\Delta c_e}$, recognizing that each is a static gain on top of $\bar{j}_-^{Li}(x,s)/\overline{I}(s)$, $\bar{j}_+^{Li}(x,s)/\overline{I}(s)$ and $\Delta\bar{c}_e(x,s)/\overline{I}(s)$ dynamics, respectively.

3. Model order reduction

3.1. Impedance model

Given a full order impedance model transfer matrix $\bar{\mathbf{y}}(s)/\overline{I}(s)$, the reduced order transfer matrix [9] is defined to be

$$\frac{\bar{\mathbf{y}}^*(s)}{\overline{I}(s)} = \mathbf{Z} + \sum_{k=1}^{n} \frac{\mathbf{r}_k s}{s - \lambda_k}. \quad (51)$$

In Eq. (51), λ_k and $\mathbf{r}_k$ are numerically generated eigenvalues and $n_x \times 1$ residue vectors, respectively. The $n_x \times 1$ steady state vector, $\mathbf{Z}$, is obtained directly from the full order model as $\mathbf{Z} = \lim_{s\to 0} \bar{\mathbf{y}}(s)/\overline{I}(s)$. Defining the error between the reduced and full order models as $\hat{\bar{\mathbf{y}}}(s) = \bar{\mathbf{y}}^*(s) - \bar{\mathbf{y}}(s)$, the remaining model parameters $\mathbf{p} = (\lambda_k, \mathbf{r}_k^T)^T$ are obtained by numerically minimizing the frequency response cost functional

$$J = \sum_{k=1}^{n_\omega} \sum_{i=1}^{n_x} |\mathrm{Re}(\hat{\bar{\mathbf{y}}}_i(j\omega_k))|^2 + \mathrm{Im}(\hat{\bar{\mathbf{y}}}_i(j\omega_k))|^2 \quad (52)$$

across the desired frequency bandwidth $\omega \in [0, 2\pi f_c]$ with n_ω observations and 1D spatial domain $x \in [0, L]$ with n_x observations. We quantify the error attributable to impedance model order reduction using error norms

$$L^2 = \left[\frac{1}{n_\omega} \sum_{k=1}^{n_\omega} \frac{1}{L} \int_0^L |\hat{\bar{y}}(x, j\omega_k)|^2 \, dx\right]^{\frac{1}{2}}, \quad L^\infty = \max_{x\in[0,L], \omega\in[0,2\pi f_c]} |\hat{\bar{y}}(x, j\omega)|. \quad (53)$$

3.2. State variable realization

Using the nth order model parameters $(\mathbf{Z}^T, \lambda_k, \mathbf{r}_k^T)^T$, we obtain the nth order time domain SVM

$$\dot{\mathbf{x}}(t) = \mathbf{A}\mathbf{x}(t) + \mathbf{B}I(t), \quad \mathbf{y}^*(t) = \mathbf{C}x(t) + \mathbf{D}I(t) \quad (54)$$

where

$$\mathbf{A} = \mathrm{diag}[\lambda_1 \cdots \lambda_n], \quad \mathbf{B} = [1 \cdots 1]^T, \quad \mathbf{C} = [\mathbf{r}_1\lambda_1 \cdots \mathbf{r}_n\lambda_n], \quad \mathbf{D} = \left[\mathbf{Z} + \sum_{k=1}^{n} \mathbf{r}_k\right]. \quad (55)$$

4. Results and discussion

To demonstrate the proposed modeling approach, we employ the impedance model (Section 2.2) with reduced order frequency and time domain realizations (Section 3) to a 6 Ah Li-ion HEV cell. Previous work [11] identified and validated a 313th order CFD model (Section 2.1) against constant current and transient pulse current experimental data from that cell. The model parameters are listed in Table 1. The higher order nonlinear CFD model is employed as a truth model for comparison with low order SVM time simulation results.

HEV cells are typically pulse charged and discharged within a narrow SOC range, perhaps 30–70%. Manufacturer specified voltage limits are 2.7 and 3.9 V for the present cell, however, for short duration pulse events, it is possible to exceed these voltage limits to as much as 2.5 and 4.3 V without encountering saturation/depletion conditions or initiating damaging side reactions. As a design goal for the present work, we attempt to create a low order SVM with 0–10 Hz bandwidth and less than 1% error in predicted voltage for any arbitrary current profile. Calculated using the lowest voltage, the worst case voltage error threshold is ±25 mV.

Following the industry convention, we use "C-rate" terminology to describe current rate capability. From the full charged (100% SOC) initial condition, a 1 C (6 A) discharge rate, for example, is sustainable for roughly 1 h, thus delivering the nameplate capacity (6 Ah). In practice,

Table 1
Model parameters for 6 Ah Li-ion HEV cell

	Parameter	Negative electrode	Separator	Positive electrode
Design specifications (geometry and volume fractions)	Thickness, δ (cm)	50×10^{-4}	25.4×10^{-4}	36.4×10^{-4}
	Particle radius, R_s (cm)	1×10^{-4}		1×10^{-4}
	Active material volume fraction, ε_s	0.580		0.500
	Polymer phase volume. fraction, ε_p	0.048	0.5	0.110
	Conductive filler volume. fraction, ε_f	0.040		0.06
	Porosity (electrolyte phase volume fraction), ε_e	0.332	0.5	0.330
Li^+ concentrations	Maximum solid phase concentration $c_{s,max}$ (mol cm^{-3})	16.1×10^{-3}		23.9×10^{-3}
	Stoichiometry at 0% SOC, $x_{0\%}$, $y_{0\%}$	0.126		0.936
	Stoichiometry at 100% SOC, $x_{100\%}$, $y_{100\%}$	0.676		0.442
	Average electrolyte concentration, c_e (mol cm^{-3})		1.2×10^{-3}	
Kinetic and transport properties	Exchange current density, i_0 (A cm^{-2})	3.6×10^{-3}		2.6×10^{-3}
	Charge-transfer coefficients, α_a, α_c	0.5, 0.5		0.5, 0.5
	SEI layer film resistance, R_{SEI} (Ω cm^2)	0		0
	Solid phase Li diffusion coefficient, D_s (cm^2 s^{-1})	2.0×10^{-12}		3.7×10^{-12}
	Solid phase conductivity, σ (S cm^{-1})	1.0		0.1
	Bruggeman porosity exponent, p	1.5	1.5	1.5
	Electrolyte phase Li^+ diffusion coefficient, D_e (cm^2 s^{-1})		2.6×10^{-6}	
	Electrolyte phase ionic conductivity, κ (S cm^{-1})		$\kappa = 15.8\ c_e\exp[0.85(1000c_e)^{1.4}]$	
	Electrolyte activity coefficient, $f_\pm$		1.0	
	Li^+ transference number, t_+^0		0.363	

	Parameter	Value
Equilibrium potential	Negative electrode, U_- (V)	$U_-(x) = 8.00229 + 5.0647x - 12.578x^{1/2} - 8.6322\times10^{-4}x^{-1} + 2.1765\times10^{-5}x^{3/2} - 0.46016\exp[15.0(0.06-x)] - 0.55364\exp[-2.4326(x-0.92)]$, where $x = c_{s,e-}/c_{s,max-}$
	Positive Electrode, U_+ (V)	$U_+(y) = 85.681y^6 - 357.70y^5 + 613.89y^4 - 555.65y^3 + 281.06y^2 - 76.648y - 0.30987\exp(5.657y^{115.0}) + 13.1983$, where $y = c_{s,e+}/c_{s,max+}$
Plate area-specific parameters	Electrode plate area, A (cm^2)	10,452
	Current collector contact resistance, R_f (Ω cm^2)	20

capacity differs from these nominal values. Table 1 defines 0 and 100% SOC stoichiometries on a 7.19 Ah basis, the actual capacity measured at the 1 C rate [11]. Ohmic and transport limitations reduce available capacity at high rates. For the present cell, a 50 C (300 A) rate is available for just 12 s from 100% SOC, having discharged only 1 Ah capacity before negative electrode solid surface concentrations become depleted.

4.1. Linear models

4.1.1. Submodel identification

Parabolic PDE systems, such as the three coupled diffusion problems considered here, are characterized by an infinite number of negative real eigenvalues, often closely spaced with similar residues. The slowest non-zero eigenvalue of the solid phase diffusion transfer function equation (16) occurs at $\lambda = D_s(\xi/R_s)$ where ξ is the first non-zero root of $\tan(\xi) = \xi$. This is also the slowest eigenvalue of transfer functions Eqs. (31)–(34). For the negative electrode, with slightly more sluggish diffusion than the positive electrode, this is $\lambda_0 = -4.04\times10^{-3}$ rad/s, or 6.4×10^{-4} Hz. Within the desired dynamic range $\lambda_0/2\pi \leqslant f \leqslant f_c = 10$ Hz, Eq. (16) in the negative electrode has 178 eigenvalues [9], while Eqs. (31)–(34) have thousands of eigenvalues. The present model order reduction procedure locates its slowest numerical eigenvalue just to the left of the slowest actual eigenvalue, with the remaining eigenvalues more or less evenly distributed in logarithmic space along the real axis to a location near $-2\pi f_c$.

To illustrate the identification procedure, Fig. 2 compares the $\bar{c}_{s,e-}(x,s)/\bar{I}(s)$ frequency response of the exact, infinite dimensional transcendental transfer function equation (34) to a 5th order rational polynomial transfer function approximation equation (51). The approximate transfer function minimizes the cost functional equation (52) in the frequency range $f = \omega/2\pi \in [0, 10\text{ Hz}]$. Note that the phase angle of the 5th order model departs from the exact value for $f > 10$ Hz. Not shown, lower order models yield visibly poorer results, alternately under predicting and over predicting magnitude and phase angle. Following the same procedure, we fit low order models to Eqs. (32) and (34) (once for each electrode) and Eq. (38) at the 50% SOC operating point. Eqs. (33) and (44) are calculated as static gains of low order models fitted to Eqs. (32) and (38).

The **A**, **B**, **C** and **D** matrices of SIMO time domain models are assembled directly from numerically identified parameters $\mathbf{Z}^T$, λ_k and $\mathbf{r}_k$ using Eq. (55). Fig. 3 shows distributions of j^{Li}, $c_{s,e}$ and c_e across the cell at various times

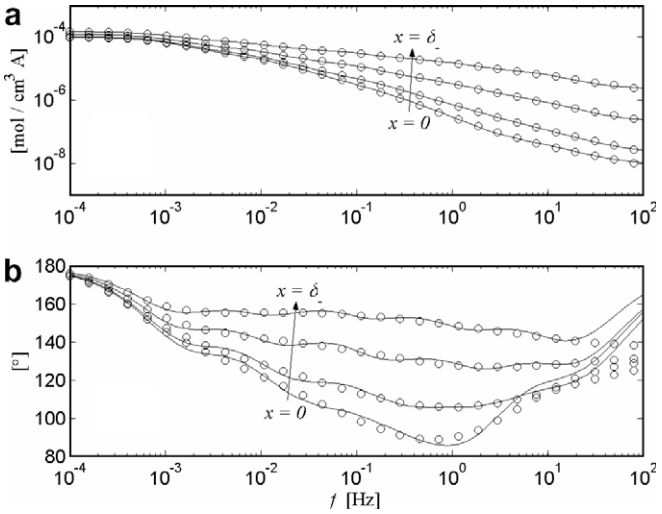

Fig. 2. Negative electrode surface concentration frequency response: Exact transfer function (○) and 5th order polynomial transfer function (–). (a) Magnitude, $|\Delta\bar{c}_{s,e-}(x,s)/\bar{I}(s)|$. (b) Phase angle, $\angle(\Delta\bar{c}_{s,e-}(x,s)/\bar{I}(s))$.

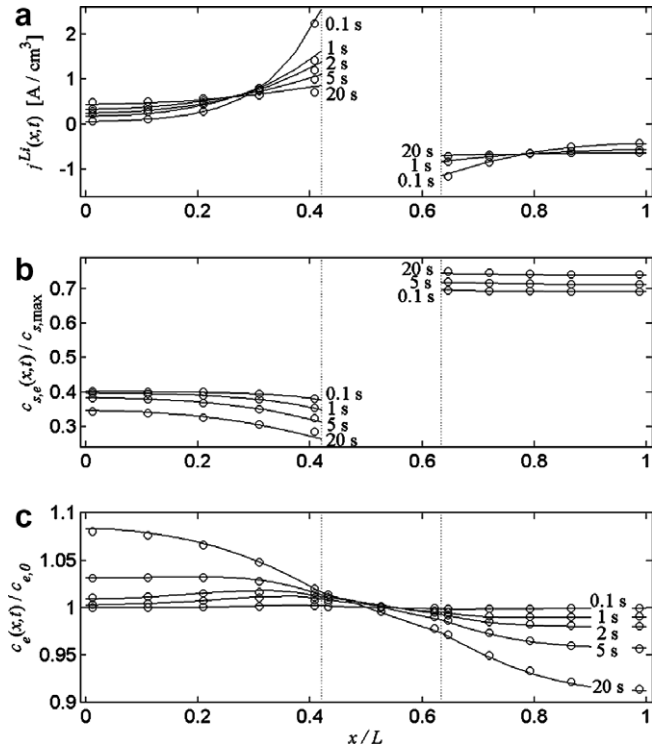

Fig. 3. Reaction and concentration distributions during 5 C discharge from 50% SOC initial condition: CFD model (○) and 5th order negative electrode/5th order positive electrode/3rd order electrolyte linear submodels (–). (a) Reaction current density. (b) Electrode surface concentration. (c) Electrolyte concentration.

during a 5 C (30 A) discharge from the 50% SOC initial condition. Initial spikes in reaction current, j^{Li}, near the separator decay as Li is de-inserted/inserted from the negative/positive electrode surface. Equilibrium potentials rise/fall most rapidly near the separator, penalizing further reaction, and over time, j^{Li} becomes more uniform. Surface concentrations, $c_{s,e}$, fall/rise in a distributed manner consistent with the time history of reaction, j^{Li}. While discharge continues, $c_{s,e}$ continues to rise/fall, and, unlike $\Delta c_{s,e}$, it never reaches steady state due to the electrode bulk concentration free integrator term Eq. (35). Shown at the bottom of Fig. 3, electrolyte concentration, c_e, does approach a steady state distribution due to offsetting source/sink terms, j^{Li}, in the negative/positive electrode regions of Eq. (4).

4.1.2. Model order selection

Choice of model order is application dependent. Accurate prediction of electrochemical field variable distributions sometimes requires higher order models than what is necessary to predict current/voltage behavior at the cell boundaries Eq. (45). Our primary focus in this paper is to predict voltage response with <25 mV error.

Transfer functions with similar eigenvalues may be fitted simultaneously and forced to share eigenvalues, reducing the number of model states. As a general approach, we create three separate reduced order submodels per Eqs. (48)–(50), and force each to share a common set of eigenvalues. We refer to them as the negative electrode submodel, positive electrode submodel, and electrolyte submodel. The open circuit voltage submodel, Eq. (47), containing a single eigenvalue at the origin, plays no role in model order reduction.

Table 2 displays error metrics of the three submodels for different choices of model order. Tabulated error values are normalized by each transfer function's steady state impedance at the current collector, $x = 0$ or L, listed in parenthesis in the left most column. L^2 and L^∞ norms equation (53) provide information on the quality of fit for 1D field variable distributions, while values listed at $x = 0$ or L quantify submodel error contributions to cell voltage response. At 50% SOC, positive electrode surface concentration represents the dominant impedance due to the strong equilibrium potential coupling, $\partial U_+/\partial c_{s+}$. Overpotential impedance is almost negligible.

For the present model to achieve <25 mV cell voltage error at the 50 C current rate requires total impedance error $<8.3\times10^{-5}\ \Omega$. Current collector errors listed in Table 2 are not strictly additive, however, as individual transfer function errors occur at different frequencies and sometimes cancel one another. For small perturbations about the 50% SOC linearization point, 3rd order electrode models are often sufficient. Sustained high rate currents are more difficult to model accurately, and in particular, to capture electrode surface saturation/depletion nonlinearities (Section 4.2) at the end of 50 C discharge, we must use 5th order models for each electrode. Much of the $\phi_e^{\Delta c_e}$ impedance is static, and we find a 1st order model of electrolyte dynamics sufficient for the present cell. Except where noted, the 5th order negative electrode, 5th order positive electrode, 1st order electrolyte model, denoted as $5D_{s-}/5D_{s+}/1D_e$, is used for all simulations. The eigenvalues are:

Table 2
Impedance error magnitude for negative electrode, positive electrode, and electrolyte submodels of various orders across frequency range $0 \leqslant f \leqslant 10$ Hz

Transfer function (steady state impedance)	Error	Negative electrode submodel order		
		3	4	5
$\lvert(\frac{\partial U_-}{\partial c_{s,-}})\Delta c_{s,e-}(x,j\omega)/I(j\omega)\rvert$ (3.65×10^{-4} Ω @ $x=0$, $\omega=0$)	$x=0$	0.1215	0.0689	0.0387
	L^∞	0.1440	0.0711	0.0453
	L^2	0.0672	0.0319	0.0175
$\lvert\eta_-(x,j\omega)/I(j\omega)\rvert$ (7.85×10^{-6} Ω @ $x=0$, $\omega=0$)	$x=0$	0.0674	0.0283	0.0159
	L^∞	0.2636	0.1030	0.0391
	L^2	0.0558	0.0227	0.0103
$\lvert\Delta\phi_e^{j_{Li}}(x,j\omega)/I(j\omega)\rvert$ (2.44×10^{-4} Ω @ $x=L$, $\omega=0$)	$x=L$	0.0473	0.0236	0.0111
	L^∞	0.0566	0.0281	0.0132
	L^2	0.0304	0.0129	0.0063
		Positive electrode submodel order		
		3	4	5
$\lvert(\frac{\partial U_+}{\partial c_{s,+}})\Delta c_{s,e+}(x,j\omega)/I(j\omega)\rvert$ (2.50×10^{-3} Ω @ $x=0$, $\omega=0$)	$x=L$	0.1203	0.0353	0.0089
	L^∞	0.1213	0.0354	0.0095
	L^2	0.0526	0.0165	0.0053
$\lvert\eta_+(x,j\omega)/I(j\omega)\rvert$ (1.45×10^{-5} Ω @ $x=0$, $\omega=0$)	$x=L$	0.0668	0.0424	0.0219
	L^∞	0.2597	0.1165	0.0724
	L^2	0.0378	0.0217	0.0108
$\lvert\Delta\phi_e^{j_{Li}}(x,j\omega)/I(j\omega)\rvert$ (2.42×10^{-4} Ω @ $x=L$, $\omega=0$)	$x=L$	0.0227	0.0141	0.0077
	L^∞	0.0227	0.0141	0.0077
	L^2	0.0049	0.0029	0.0014
		Electrolyte submodel order		
		1	2	3
$\lvert\Delta\phi_e^{\Delta c_e}(x,j\omega)/I(j\omega)\rvert$ (2.13×10^{-4} Ω @ $x=L$, $\omega=0$)	$x=L$	0.0555	0.0447	0.0365
	L^∞	0.1123	0.0944	0.0407
	L^2	0.0318	0.0255	0.0155

Local error quantified at the current collector appropriate for the given submodel, either $x=0$ or $x=L$. Distributed error quantified with L^∞ and L^2 error norms, Eq. (53). All errors normalized by steady state impedance at the current collector.

Table 3
Impedance error magnitude for combined negative electrode/positive electrode submodels (with common eigenvalues) of various orders across frequency range $0 \leqslant f \leqslant 10$ Hz

Transfer function (steady state impedance)	Error	Negative/positive electrode submodel order		
		3	4	5
$\lvert(\frac{\partial U_-}{\partial c_{s,-}})\Delta c_{s,e-}(x,j\omega)/I(j\omega)\rvert$ (3.65×10^{-4} Ω @ $x=0$, $\omega=0$)	$x=0$	0.2330	0.1410	0.1089
	L^∞	0.2425	0.1529	0.1199
	L^2	0.1005	0.0581	0.0453
$\lvert\eta_-(x,j\omega)/I(j\omega)\rvert$ (7.85×10^{-6} Ω @ $x=0$, $\omega=0$)	$x=0$	0.0559	0.0273	0.0161
	L^∞	0.2485	0.1043	0.0421
	L^2	0.0495	0.0227	0.0111
$\lvert\Delta\phi_e^{j_{Li}}(x,j\omega)/I(j\omega)\rvert$ (2.44×10^{-4} Ω @ $x=L$, $\omega=0$)	$x=L$	0.0389	0.0229	0.0112
	L^∞	0.0478	0.0276	0.0132
	L^2	0.0261	0.0128	0.0067
$\lvert(\frac{\partial U_+}{\partial c_{s,+}})\Delta c_{s,e+}(x,j\omega)/I(j\omega)\rvert$ (2.50×10^{-3} Ω @ $x=0$, $\omega=0$)	$x=L$	0.1086	0.0787	0.0534
	L^∞	0.1086	0.0803	0.0534
	L^2	0.0481	0.0327	0.0219
$\lvert\eta_+(x,j\omega)/I(j\omega)\rvert$ (1.45×10^{-5} Ω @ $x=0$, $\omega=0$)	$x=L$	0.0744	0.0417	0.0198
	L^∞	0.2078	0.1139	0.0675
	L^2	0.0411	0.0212	0.0099
$\lvert\Delta\phi_e^{j_{Li}}(x,j\omega)/I(j\omega)\rvert$ (2.42×10^{-4} Ω @ $x=L$, $\omega=0$)	$x=L$	0.0252	0.0137	0.0070
	L^∞	0.0252	0.0137	0.0070
	L^2	0.0054	0.0028	0.0013

Local error quantified at the current collector appropriate for the given submodel, either $x=0$ or $x=L$. Distributed error quantified with L^∞ and L^2 error norms, Eq. (53). All errors normalized by steady state impedance at the current collector.

$$\lambda_- = -[0.0050, 0.0605, 0.06576, 6.3763, 62.43] \quad \text{rad/s}$$
$$\lambda_+ = -[0.0085, 0.0608, 0.05691, 5.8226, 63.69] \quad \text{rad/s}$$
$$\lambda_e = -0.098 \quad \text{rad/s}$$

Including open circuit potential submodel equation (47) with $\lambda_{OC}=0$, the complete cell model is 12th order.

Before proceeding, we note that lower order SVMs may be obtained by forcing submodels to share eigenvalues. By simultaneously fitting negative and positive electrode transfer functions, we may replace eigenvalues λ_- and λ_+ with a single set of eigenvalues, $\lambda_\pm$. This order reduction is achieved at the expense of increased impedance error quantified in Table 3.

4.1.3. Current/voltage model

The current/voltage model is a state variable realization of Eq. (46) with reduced order submodels identified as described in Sections 4.1.1 and 4.1.2. Unlike the transfer function equation (46), the SVM may take on non-zero initial conditions for $c_{s,avg-}$ and $c_{s,avg+}$. Following typical convention, we define SOC as the fraction of capacity, Q, stored in the cell. Given an initial SOC at $t=0$ and assuming 100% coulombic efficiency, SOC may be calculated in time as

$$\mathrm{SOC}(t) = -\frac{1}{Q}\int_0^t I(t)\,\mathrm{d}t. \tag{56}$$

We express $c_{s,avg-} = f(\mathrm{SOC})$ and $c_{s,avg+} = f(\mathrm{SOC})$ by defining a reference stoichiometry, $\theta = c_{s,avg}/c_{s,max}$, for each electrode at the 100% SOC condition, $\theta_{100\%}$, listed in Table 1. The 0% SOC reference stoichiometry, $\theta_{0\%}$, is calculated by subtracting $Q = 7.19$ Ah from $\theta_{100\%}$ with appropriate units conversion,

$$\theta_{0\%} = \theta_{100\%} - Q\left(\frac{1}{AF}\frac{1}{\delta\varepsilon_s}\frac{1}{c_{s,\max}}\right). \tag{57}$$

With reference stoichiometries, we may express each electrode's bulk concentration as a linear function of SOC,

$$c_{s,avg}(t) = [\mathrm{SOC}(t)(\theta_{100\%} - \theta_{0\%}) + \theta_{0\%}]c_{s,\max}, \tag{58}$$

valid at any point in time.

Linearized about 50% SOC, the linear current/voltage SVM is

$$\frac{\mathrm{d}}{\mathrm{d}t}\begin{bmatrix}\mathrm{SOC}\\ \mathbf{x}_-\\ \mathbf{x}_+\\ \mathbf{x}_\mathrm{e}\end{bmatrix}=\begin{bmatrix}0 & & & \\ & \mathbf{A}_- & & \\ & & \mathbf{A}_+ & \\ & & & \mathbf{A}_\mathrm{e}\end{bmatrix}\begin{bmatrix}\mathrm{SOC}\\ \mathbf{x}_-\\ \mathbf{x}_+\\ \mathbf{x}_\mathrm{e}\end{bmatrix}+\begin{bmatrix}-\frac{1}{Q}\\ 1\\ \vdots\\ 1\end{bmatrix}I(t)$$

$$V(t)=\begin{bmatrix}\frac{\partial V_\mathrm{OC}}{\partial \mathrm{SOC}} & \mathbf{C}_- & \mathbf{C}_+ & \mathbf{C}_\mathrm{e}\end{bmatrix}\begin{bmatrix}\mathrm{SOC}\\ \mathbf{x}_-\\ \mathbf{x}_+\\ \mathbf{x}_\mathrm{e}\end{bmatrix}+\left[\mathbf{D}_-+\mathbf{D}_++\mathbf{D}_\mathrm{e}-\frac{R_\mathrm{f}}{A}\right]I(t)+V_\mathrm{static} \tag{59}$$

where

$$\mathbf{C}_-=\mathbf{C}^{\Delta c_{\mathrm{s,e}-}}+\mathbf{C}^{\eta_-}+\mathbf{C}^{\Delta\phi_\mathrm{e}^{j_-^\mathrm{Li}}} \qquad \mathbf{D}_-=\mathbf{D}^{\Delta c_{\mathrm{s,e}-}}+\mathbf{D}^{\eta_-}+\mathbf{D}^{\Delta\phi_\mathrm{e}^{j_-^\mathrm{Li}}}$$

$$\mathbf{C}_+=\mathbf{C}^{\Delta c_{\mathrm{s,e}+}}+\mathbf{C}^{\eta_+}+\mathbf{C}^{\Delta\phi_\mathrm{e}^{j_+^\mathrm{Li}}} \qquad \mathbf{D}_+=\mathbf{D}^{\Delta c_{\mathrm{s,e}+}}+\mathbf{D}^{\eta_+}+\mathbf{D}^{\Delta\phi_\mathrm{e}^{j_+^\mathrm{Li}}}$$

$$\mathbf{C}_\mathrm{e}=\mathbf{C}^{\Delta\phi_\mathrm{e}^{\Delta c_\mathrm{e}}} \qquad \mathbf{D}_\mathrm{e}=\mathbf{D}^{\Delta\phi_\mathrm{e}^{\Delta c_\mathrm{e}}} \tag{60}$$

$$\frac{\partial V_\mathrm{OC}}{\partial \mathrm{SOC}}=\frac{Q}{AF}\left(\left.\frac{\partial U_+}{\partial c_{s+}}\right|_{50\%}\frac{1}{\delta_+\varepsilon_{s+}}-\left.\frac{\partial U_-}{\partial c_{\mathrm{s}-}}\right|_{50\%}\frac{1}{\delta_-\varepsilon_{\mathrm{s}-}}\right) \tag{61}$$

$$V_\mathrm{static}|_{50\%}=U_+|_{50\%}-U_-|_{50\%}-0.5\left.\frac{\partial V_\mathrm{OC}}{\partial \mathrm{SOC}}\right|_{50\%}. \tag{62}$$

Fig. 4 compares the voltage response of the $5D_{\mathrm{s}-}/5D_{\mathrm{s}+}/1D_\mathrm{e}$ linear SVM to the nonlinear CFD model for a stepped current profile at the 50% SOC initial condition. The current profile, serving as input to both models, consists of 10 C, 20 C, 30 C and 40 C discharge/charge/rest cycles. Each discharge/charge cycle returns the cell to 50% SOC. Voltage prediction for the linear SVM is reasonably good, although we see from Fig. 4d that individual submodel errors cancel one another throughout much of the profile. Submodel errors worsen with increasing current rate as electrode surface concentrations are perturbed far from the 50% SOC linearization point.

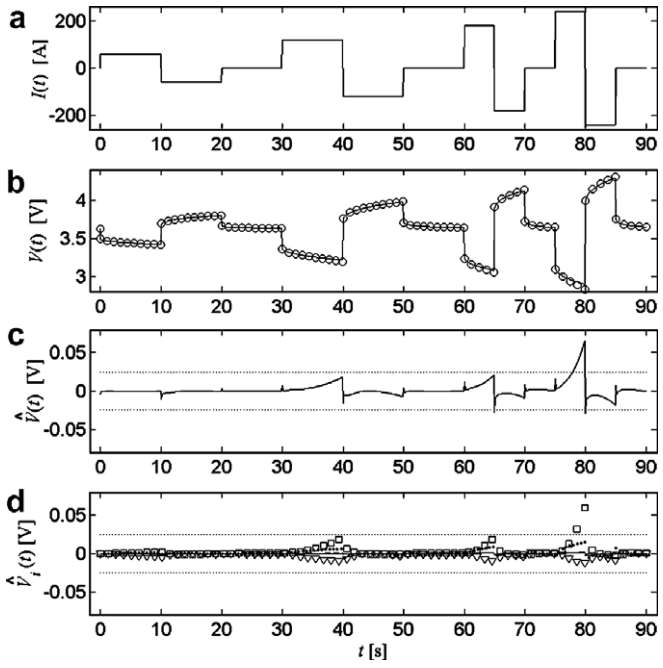

Fig. 4. Linear SVM voltage response and error for pulse current profile at 50% SOC. (a) Current profile. (b) Voltage response of CFD model (○) and linear SVM (–). (c) Voltage response error of linear SVM (–) with 25 mV error threshold (···). (d) Individual submodel contributions to voltage error: $\hat{\eta}_-(0,t)$ (——), $\hat{\eta}_+(L,t)$ (---), $\hat{U}_-(0,t)$ (□), $\hat{U}_+(L,t)$ (▽), $\Delta\hat{\phi}_\mathrm{e}(L,t)$ (●), with 25 mV error threshold (···).

4.1.4. Observability and controllability properties

Using standard techniques [22], we assemble observability

$$\vartheta_0=\begin{bmatrix}\mathbf{C}^\mathrm{T} & (\mathbf{CA})^\mathrm{T} & (\mathbf{CA}^2)^\mathrm{T} & \cdots & (\mathbf{CA}^{n-1})^\mathrm{T}\end{bmatrix}^\mathrm{T} \tag{63}$$

and controllability

$$\vartheta_\mathrm{c}=\begin{bmatrix}\mathbf{A} & \mathbf{AB} & \mathbf{A}^2\mathbf{B} & \cdots & \mathbf{A}^{n-1}\mathbf{B}\end{bmatrix}. \tag{64}$$

matrices. Both have full rank, indicating that the model is fully observable and controllable.

Some model states may be less observable/controllable than others, which we quantify using the observability/controllability gramian of a balanced realization model. We define an observability gramian, $\mathbf{W}_\mathrm{o}$, as the solution to

$$\mathbf{A}^\mathrm{T}\mathbf{W}_\mathrm{o}+\mathbf{W}_\mathrm{o}\mathbf{A}+\mathbf{C}^\mathrm{T}\mathbf{C}=0 \tag{65}$$

and the controllability gramian, $\mathbf{W}_\mathrm{c}$, as the solution to

$$\mathbf{AW}_\mathrm{c}+\mathbf{W}_\mathrm{c}\mathbf{A}^\mathrm{T}+\mathbf{BB}^\mathrm{T}=0. \tag{66}$$

Applying transformation $\bar{\mathbf{x}}=\mathbf{Tx}$, an alternative realization of the SVM is

$$\begin{aligned}\dot{\bar{\mathbf{x}}}&=\mathbf{TAT}^{-1}\bar{\mathbf{x}}+\mathbf{TB}I\\ y&=\mathbf{CT}^{-1}\bar{\mathbf{x}}+\mathbf{D}I\end{aligned} \tag{67}$$

with observability and controllability gramians, $\overline{\mathbf{W}}_\mathrm{o}=\mathbf{T}^{-T}\mathbf{W}_\mathrm{o}\mathbf{T}^{-1}$ and $\overline{\mathbf{W}}_\mathrm{c}=\mathbf{TW}_\mathrm{c}\mathbf{T}^\mathrm{T}$, respectively. The balanced realization of Eq. (67) results when transform matrix $\mathbf{T}$ is such that $\overline{\mathbf{W}}_\mathrm{o}=\overline{\mathbf{W}}_\mathrm{c}=\mathrm{diag}(\mathbf{g})$.

Table 4 presents the observability/controllability gramian of the balanced realization $5D_{\mathrm{s}-}/5D_{\mathrm{s}+}/1D_\mathrm{e}$ linear SVM. Fast electrode states are most observable/controllable. This is intuitive, as the rapid perturbations in electrode

Table 4
Observability/controllability gramian of balanced realization $5D_{\mathrm{s}-}/5D_{\mathrm{s}+}/1D_\mathrm{e}$ SVM linearized at 50% SOC

	Eigenvalue, λ_k (rad/s)	Gramian, g_k ($(\Omega\,\mathrm{s})^{1/2}$)
Negative electrode submodel	-5.56×10^{-3}	4.33×10^{-8}
	-6.05×10^{-2}	4.39×10^{-12}
	-6.58×10^{-1}	6.31×10^{-6}
	-6.38	4.34×10^{-5}
	-62.4	1.146×10^{-4}
Positive electrode submodel	-8.53×10^{-3}	2.07×10^{-6}
	-6.08×10^{-2}	2.16×10^{-10}
	-5.69×10^{-1}	2.98×10^{-6}
	-5.82	1.400×10^{-5}
	-63.7	7.42×10^{-4}
Electrolyte submodel	-9.49×10^{-1}	7.54×10^{-9}

surface concentration (of which voltage response is a strong function) are predominantly influenced by recent current history. In contrast, electrode bulk concentrations (i.e. SOC) rise and fall slowly and are weakly coupled to voltage response. For estimation/control schemes in fast dynamic applications, it may be possible to reduce order by dropping slow electrode states with weak observability/controllability. The electrolyte submodel state is also weakly observable/controllable, indicating that it will probably be difficult to ascertain electrolyte concentration gradients using a linear observer. Nonetheless, the results are encouraging. To date, the battery estimation literature has predominantly focused on SOC estimation. In high power, pulse type applications, however, it is attractive to estimate electrode surface concentrations, as their saturation/depletion are responsible for sudden loss of power and side reactions. Table 4 indicates that electrode surface concentrations are more controllable/observable than SOC.

4.2. Nonlinear models

Concentration dependent properties represent the dominant nonlinearities in Eqs. (1)–(15). Those appearing explicitly in the output equation of Eq. (59) are readily included in the SVM. Other nonlinearities exhibit complex spatial dependency that we approximate on an electrode averaged, or lumped basis.

4.2.1. Open circuit potential

The open circuit potential (OCP) nonlinearity is incorporated by introducing equilibrium potential relationships, $U_+(c_{s,e}(L,t))$ and $U_-(c_{s,e}(0,t))$ listed in Table 1, into the model output equation. The nonlinear SVM takes the form

$$\begin{aligned}\dot{\mathbf{x}} &= \mathbf{A}\mathbf{x} + \mathbf{B}I \\ V &= h(\mathbf{x}, I)\end{aligned} \tag{68}$$

Unlike the linear SVM, the nonlinear OCP SVM correctly predicts battery rest voltage, or open circuit voltage (OCV) at all values of SOC. Dynamic response is still lacking, however.

Fig. 5 shows the voltage response for constant current (1–50 C) discharge simulations initiated from 0% depth of discharge (DOD), i.e. 100% SOC, as predicted by the CFD model, linear SVM Eq. (59) and nonlinear OCP SVM. At low current rates, the linear SVM gives reasonable approximation only in the middle of the discharge as surface concentrations $c_{s,e}(0,t)$ and $c_{s,e}(L,t)$ pass through their 50% SOC linearization point. The nonlinear OCP SVM greatly improves voltage prediction over the linear model at the beginning of discharge, near 100% SOC. The end of discharge voltage prediction is poor, however, for all but the lowest rate, the 1 C case.

4.2.2. Electrode surface concentration

End of discharge voltage may be substantially improved by switching between local linear models identified at various electrode surface concentration set points. Voltage response predicted by the nonlinear OCP/$c_{s,e}$ SVM, shown in Fig. 5 with the "·" symbol, lays almost directly on top of the CFD model results. Unlike Sec. 4.2.1, the nonlinear OCP/$c_{s,e}$ SVM approximates $c_{s,e}(0,t)$ and $c_{s,e}(L,t)$ with nonlinear, rather than linear models.

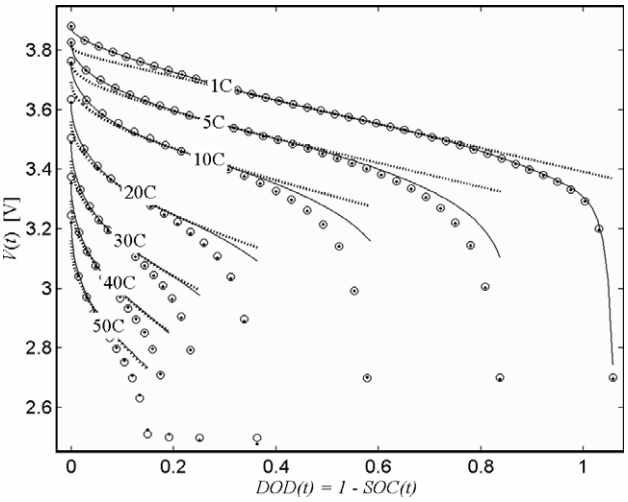

Fig. 5. Voltage response of various SVMs versus CFD model during constant current discharge from 100% SOC initial condition: CFD model (○), linear SVM (···), nonlinear OCP SVM (–), and nonlinear OCP/$c_{s,e}$ SVM (•).

Shown in Fig. 6, local electrode submodels are identified at roughly 20% increments in surface stoichiometry, with finer discretization in less linear regions of $U_+(c_{s,e}(L,t))$ and $U_-(c_{s,e}(0,t))$. There is negligible advantage in allowing each localized electrode submodel its own independent eigenvalues. We obtain good impedance fits at all set points utilizing the eigenvalues identified at 50% SOC. **A** and **B** matrices of Eq. (59), thus, remain constant. The **C** and **D** matrices vary by interpolating between locally identified electrode submodels as a function of solid phase surface concentration averaged across each electrode,

$$\begin{aligned}\mathbf{C}_- &= \mathbf{C}_-(c_{s,e\ avg-}) \quad \mathbf{D}_- = \mathbf{D}_-(c_{s,e\ avg-}) \\ \mathbf{C}_+ &= \mathbf{C}_+(c_{s,e\ avg+}) \quad \mathbf{D}_+ = \mathbf{D}_+(c_{s,e\ avg+})\end{aligned} \tag{69}$$

The nonlinear OCP/$c_{s,e}$ SVM keeps the form of Eq. (68).

Fig. 7 elucidates the substantial improvement in end of discharge voltage prediction at the 50 C rate (Fig. 5) achieved by approximating $c_{s,e}$ nonlinearities. Comparing surface concentrations predicted by the CFD model, linear model and nonlinear $c_{s,e}$ model, there is little difference between the three in the positive electrode. In the negative electrode however, the relatively flat U_- relationship at moderate to high surface stoichiometries causes reaction to be heavily favored near the separator at short times. At $t = 6$ s, the CFD model shows surface concentrations drastically different from that of the linear model. Around this time, local values of $c_{s,e-}$ fall below $\sim 0.2 c_{s,max}$, causing U_- to rise sharply (Fig. 6). At $t = 13$ s, surface concentrations are near uniformly depleted across the negative electrode, a condition accurately captured by the nonlinear $c_{s,e}$

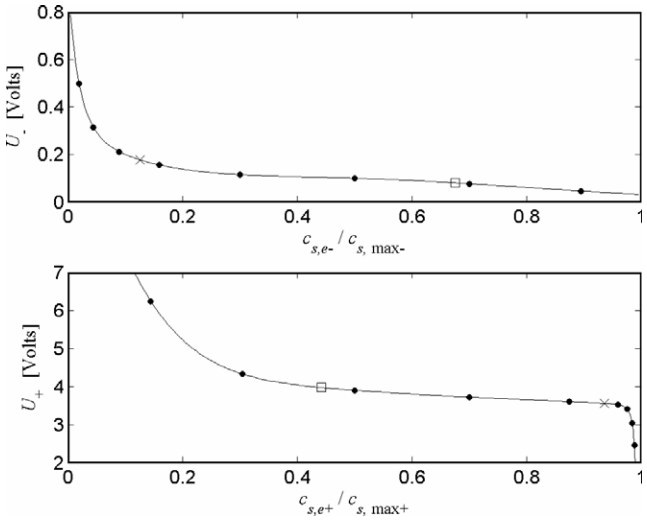

Fig. 6. Equilibrium (or open circuit) potential versus electrode surface concentration: Empirical relationships, U, from Table 1 (–), linearization set points used for nonlinear $c_{s,e}$ SVM submodel identification (●), 100% SOC reference (□) and 0% SOC reference (x).

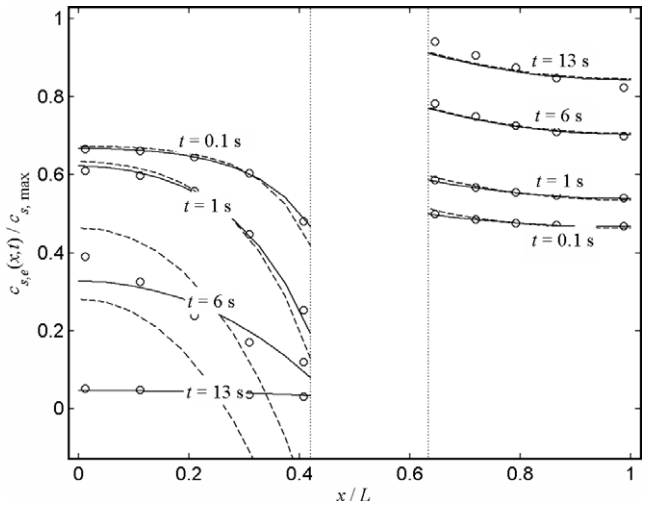

Fig. 7. Distribution of electrode surface concentration at various times during 50 C discharge from 100% SOC initial condition (voltage response shown in Fig. 5): CFD model (○), linear SVM (–), and nonlinear $c_{s,e}$ SVM (–).

model. The linear model, predicting local concentrations less than zero, is physically unrealistic.

Fig. 8 displays cell voltage error and submodel voltage error for the nonlinear OCP/$c_{s,e}$ SVM during the same 50 C discharge from 100% SOC. Equilibrium potentials at the current collectors, $U_+(c_{s,e}(L, t))$ and $U_-(c_{s,e}(0, t))$, are predicted to within 25 mV. Electrolyte phase potential error continually grows throughout the discharge, however, as a large electrolyte concentration gradient builds across the cell. Non-uniform $c_e(x, t)$ increases the significance of the electrolyte conductivity concentration dependence, $\kappa^{eff}(c_e)$.

Fig. 9 displays voltage errors for the nonlinear OCP/$c_{s,e}$ SVM in simulating the 50% SOC pulse current profile from

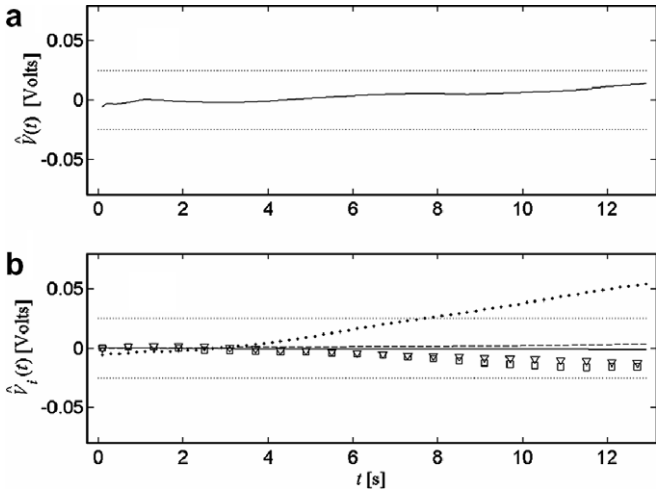

Fig. 8. Nonlinear OCP/$c_{s,e}$ SVM error during 50 C discharge from 100% SOC initial condition (voltage response shown in Fig. 5): (a) voltage response error (–) with 25 mV error threshold (···). (b) Individual submodel contributions to voltage error: $\hat{\eta}_-(0,t)$ (——), $\hat{\eta}_+(L,t)$ (---), $\widehat{U}_-(0,t)$ (□), $\widehat{U}_+(L,t)$ (▽), $\Delta\hat{\phi}_e(L,t)$ (●), with 25 mV error threshold (···).

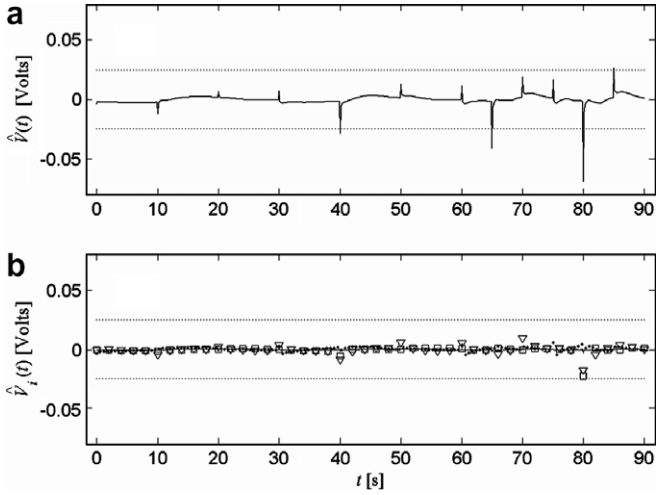

Fig. 9. Nonlinear OCP/$c_{s,e}$ SVM error during pulse current profile at 50% SOC (current profile and CFD model voltage response shown in Figs. 4a and b): (a) voltage response error (–) with 25 mV error threshold (···). (b) Individual submodel contributions to voltage error: $\hat{\eta}_-(0,t)$ (——), $\hat{\eta}_+(L,t)$ (---), $\widehat{U}_-(0,t)$ (□), $\widehat{U}_+(L,t)$ (▽), $\Delta\hat{\phi}_e(L,t)$ (●), with 25 mV error threshold (···).

Fig. 4. Here, the cell is alternately discharged and charged by short pulses, no substantial electrolyte concentration gradient is established and electrolyte phase potential error is negligible. Rapid reversals in current cause brief spikes in cell voltage error >25 mV at 40, 65 and 80 s, which quickly dissipate. Individual submodel errors are now all <25 mV, a large improvement over the linear SVM results shown in Fig. 4.

4.2.3. Electrolyte concentration

The impedance model assumption of $j^{Li}(x, t)$ decoupled from $c_e(x, t)$ loses validity as $c_e \to 0$, a condition that we explore here. With $j^{Li}(x, t)$ and $c_e(x, t)$ provided by our

linear model, it is possible to solve explicitly for $\phi_e(L, t)$ by twice integrating Eq. (9),

$$\Delta\phi_e(L,t) = \frac{2RT(t_+^0 - 1)}{F} \ln\left(\frac{c_e(0,t)}{c_e(L,t)}\right) - \int_0^L \frac{1}{\kappa^{\text{eff}}(c_e(x,t))} \int j^{\text{Li}}(x,t)\,dx\,dx, \quad (70)$$

valid for constant t_+^0 and $f_\pm$. (See Ref. [23] for discussion of non-constant t_+^0 and $f_\pm$.) For brevity, we refer to term 1 on the right hand side of Eq. (70) as the $\ln(c_e)$ nonlinearity and term 2 as the $\kappa^{\text{eff}}(c_e)$ nonlinearity. Each is a modification of the output equation of Eq. (59) with nonlinear SVM realization equation (68).

The present cell model with parameters listed in Table 1 does not experience electrolyte depletion at any current rate, however, other cells with less porous electrodes and separator may experience this limitation. To examine voltage response with end of discharge induced by electrolyte depletion, we reduce the electrolyte diffusion coefficient by one order of magnitude to $D_e = 2.6 \times 10^{-7}$ cm^2/s.

Fig. 10 presents the voltage response of this electrolyte transport limited cell for 10–50 C constant current discharge cases initiated from 100% SOC. Rate capability is substantially reduced compared to the nominal D_e model (Fig. 5). Fig. 10 shows the nonlinear OCP/$c_{s,e}$ SVM (Section 4.2.2) over predicts voltage and fails to capture end of discharge caused by electrolyte depletion. Introduction of the $\kappa^{\text{eff}}(c_e)$ nonlinearity, slightly improves voltage prediction at intermediate times, however, the end of discharge prediction remains poor. Voltage prediction degrades when the $\ln(c_e)$ nonlinearity is included, as it is very sensitive to small errors in absolute (not relative) values of $c_e(0, t)$ and $c_e(L, t)$.

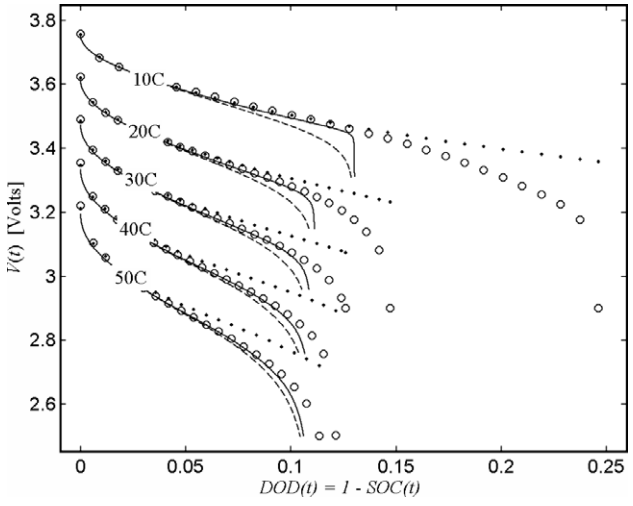

Fig. 10. Voltage response of various $5D_{s-}/5D_{s+}/3D_e$ SVMs versus CFD model during constant current discharge from 100% SOC initial condition with sluggish electrolyte diffusion, $D_e = 2.6 \times 10^{-7}$ cm^2/s: CFD model (○), nonlinear OCP/$c_{s,e}$ SVM (•), nonlinear OCP/$c_{s,e}$/$\kappa^{\text{eff}}(c_e)$ SVM (–), and nonlinear OCP/$c_{s,e}$/$\kappa^{\text{eff}}(c_e)$/$\ln(c_e)$ SVM (––).

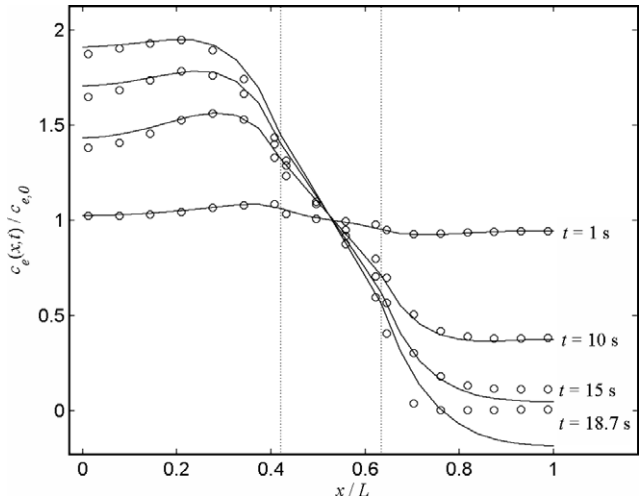

Fig. 11. Distribution of electrolyte surface concentration at various times during 30 C discharge from 100% SOC initial condition with sluggish electrolyte diffusion, $D_e = 2.6 \times 10^{-7}$ cm^2/s (voltage response shown in Fig. 10): CFD model (○) and 3rd order linear D_e submodel (–).

To elucidate these errors, Fig. 11 shows electrolyte concentration distributions at various times during the 30 C discharge case. During discharge of a cell with sluggish electrolyte transport, electrolyte depletion occurs first at $x = L$ and then spreads back across the positive electrode. Early in the discharge, the linear model predicts $c_e(x, t)$ to good accuracy, however around $t = 15$ s (corresponding to ~10% DOD in Fig. 10), the linear model begins to substantially under predict $c_e(L, t)$. By $t = 18.7$ s, the linear model predicts negative values of c_e, which are physically impossible. Extending the SVM to cover electrolyte depletion may require online PDE solution, as nonlinearities governing the j^{Li} distribution are highly spatially dependent and do not appear conducive to a lumped parameter approach. However, provided local values of c_e remain above 0.15 $c_{e,0}$, the present impedance model assumptions are valid and the nonlinear OCP/$c_{s,e}$/$\kappa^{\text{eff}}(c_e)$ SVM predicts voltage response to within 25 mV regardless of sluggish or facile D_e.

5. Conclusions

This paper numerically derives a fully observable/controllable state variable model from an impedance representation of electrochemical kinetic, species and charge conservation equations governing discharge/charge behavior of a Li-ion cell. Validated against a 313th order nonlinear CFD model of a 6 Ah HEV cell, a 12th order state variable model, with 0–10 Hz bandwidth, predicts terminal voltage to within 1% for pulse and constant current profiles at rates up to 50 C. Model properties indicate that electrode surface concentrations (with fast dynamics related to sudden loss of power and side reactions) are more observable/controllable than electrode bulk concentrations (SOC).

The state equation has a modal form with negative real eigenvalues distributed in frequency between the slowest system eigenvalue (negative electrode solid state diffusion) and 10 Hz. A single eigenvalue at the origin represents SOC dynamics. The model order reduction procedure is somewhat insensitive to numerical eigenvalue location (given the thousands of actual system eigenvalues), and we can approximate the range of admissible electrode surface concentrations using local linear models sharing a single set of eigenvalues. Open circuit potential, electrode surface concentration/reaction distribution coupling and electrolyte concentration/ionic conductivity nonlinearities are explicitly approximated in the model output equation on a local, electrode averaged and distributed basis, respectively.

The work highlights challenges associated with control oriented modeling of infinite dimensional nonlinear distributed parameters systems. We quantify error attributable to rational approximation of infinite dimensional processes in the frequency domain using impedance error norms. Errors attributable to model assumptions and lumped approximation of spatially varying nonlinearities are quantified in the time domain using the CFD model. By inducing sluggish electrolyte transport, we show the present model loses validity near electrolyte depletion ($c_e < 0.15\ c_{e,0}$) where the system exhibits strong spatially varying nonlinearities.

Acknowledgements

This work was performed at the Pennsylvania State University Electrochemical Engine Center. The authors gratefully acknowledge funding provided by the U.S. Department of Energy Graduate Automotive Technology Education (G.A.T.E.) program through the Pennsylvania Transportation Institute.

References

[1] Verbrugge M, Koch B. Generalized recursive algorithm for adaptive multiparameter regression. J Electrochem Soc 2006;153:A187–201.
[2] Pascoe PE, Anbuky AH. A unified discharge voltage characteristic for VRLA battery capacity and reserve time estimation. Energ Convers Manage 2004;45:277–302.
[3] Buller S, Thele M, De Doncker RW, Karden E. Impedance-based simulation models of supercapacitors and Li-ion batteries for power electronics applications. IEEE Trans Ind Appl 2005;41:742–7.
[4] Piller S, Perrin M, Jossen A. Methods for state-of-charge determination and their applications. J Power Sources 2001;96:113–20.
[5] Plett GL. Extended Kalman filtering for battery management systems of LiPB-based HEV battery packs – Part 3. state and parameter estimation. J Power Sources 2004;134:277–92.
[6] Junping W, Quanshi C, Binggang C. Support vector machine based battery model for electric vehicles. Energ Convers Manage 2006;47:858–64.
[7] Tenno A, Tenno R, Suntio T. Charge–discharge behaviour of VRLA batteries: model calibration and application for state estimation and failure detection. J Power Sources 2001;103:42–53.
[8] Barbarisi O, Vasca F, Glielmo L. State of charge Kalman filter estimator for automotive batteries. Control Eng Pract 2006;14:267–75.
[9] Smith KA, Rahn CD, Wang C-Y. Model order reduction of 1-D diffusion systems via residue grouping. ASME J Dyn Sys, Meas Control [in press].
[10] Karden E, Buller S, De Doncker RW. A frequency-domain approach to dynamical modeling of electrochemical power sources. Electrochim Acta 2002;47:2347–56.
[11] Smith KA, Wang C-Y. Solid state diffusion limitations on pulse operation of a lithium ion cell for hybrid electric vehicles. J Power Sources 2006;161:628–39.
[12] Chen M, Rincón-Mora GA. Accurate electrical battery model capable of predicting runtime and I–V performance. IEEE Trans Energ Convers 2006;21:504–11.
[13] Schweighofer B, Raab KM, Brasseur G. Modeling of high power automotive batteries by use of an automated test system. IEEE Trans Instrum Meas 2003;52:1087–91.
[14] Doyle M, Fuller T, Newman J. Modeling of galvanostatic charge and discharge of the lithium/polymer/insertion cell. J Electrochem Soc 1993;140:1526–33.
[15] Fuller T, Doyle M, Newman J. Simulation and optimization of the dual lithium ion insertion cell. J Electrochem Soc 1994;141:1–10.
[16] Christophides PD. Nonlinear and robust control of PDE systems – methods and applications to transport-reaction processes. Boston: Birkhauser; 2001.
[17] Park HM, Cho DH. The use of the Karhunen–Loève decomposition for the modeling of distributed parameter systems. Chem Eng Sci 1996;51:81–98.
[18] Doyle M, Meyers J, Newman J. Computer simulations of the impedance response of lithium rechargeable batteries. J Electrochem Soc 2000;147:99–110.
[19] Jacobsen T, West K. Diffusion impedance in planar, cylindrical and spherical geometry. Electrochim Acta 1995;40:255–62.
[20] Ong I, Newman J. Double-layer capacitance in a dual lithium ion insertion cell. J Electrochem Soc 1999;146:4360–5.
[21] Baker AJ, Pepper DW. Finite elements 123. New York: McGraw-Hill; 1991.
[22] Chen CT. Linear system theory and design. New York: Oxford University Press; 1999.
[23] Valøen LO, Reimers JN. Transport properties of $LiPF_6$-based electrolytes. J Electrochem Soc 2005;152:A882–91.